Adaptive Manipulation of Conductive, Nonmagnetic Objects via a Continuous Model of Magnetically Induced Force and Torque

Griffin F. Tabor*, Lan N. Pham*†, Jake J. Abbott*, Tucker Hermans*‡
*University of Utah Robotics Center, Salt Lake City, UT, USA
{griffin.tabor, jake.abbott, tucker.hermans}@utah.edu
†Relativity Space, Long Beach, CA, USA
lpham@relativityspace.com
‡NVIDIA, Seattle, WA, USA

***Abstract*—This paper extends recent work in demonstrating magnetic manipulation of conductive, nonmagnetic objects using rotating magnetic dipole fields. The current state of the art demonstrates dexterous manipulation of solid copper spheres with all object parameters known *a priori*. Our approach expands the previous model that contained three discrete modes to a single, continuous model that covers all possible relative positions of the manipulated object relative to the magnetic field source. We further leverage this new model to examine manipulation of spherical objects with unknown physical parameters, by applying techniques from the online-optimization and adaptive-control literature. Our experimental results validate our new dynamics model, showing that we get comparable or improved performance to the previously proposed model, while solving a simpler optimization problem for control. We further demonstrate the first physical magnetic control of aluminum spheres, as previous controllers were only physically validated on copper spheres. We show that our adaptive control framework can quickly acquire accurate estimates of the true spherical radius when weakly initialized, enabling control of spheres with unknown physical properties. Finally, we demonstrate that the spherical-object model can be used as an approximate model for adaptive control of nonspherical objects by performing the first magnetic manipulation of nonspherical, nonmagnetic objects.**

I. INTRODUCTION

There have been significant advances on the topic of magnetic manipulation over the past decade, the vast majority coming from the robotics community [1]. Researchers have developed methods to use sets of stationary electromagnets, or robot-controlled permanent magnets, to dexterously manipulate both tethered and untethered devices without any direct physical contact. However, the objects being manipulated have typically comprised a large fraction of ferromagnetic material (soft- or permanent-magnet). This severely limits the types of objects that can be manipulated using magnetic methods that are based on ferromagnetism, since ultimately a very limited set of materials exhibit ferromagnetism.

Many engineering materials, although not ferromagnetic, are electrically conductive, including aluminum, titanium, copper, and some stainless steels. It has long been known that when conductive objects are exposed to time-varying magnetic fields (as opposed to static magnetic fields), a flow of electrons known as eddy currents is induced in the material [5]. These eddy currents produce their own magnetic fields, which then interact with the applied magnetic field, inducing forces and torques on the conductive object. A common commercial applications of this phenomenon is material separation in metal recycling plants [24].

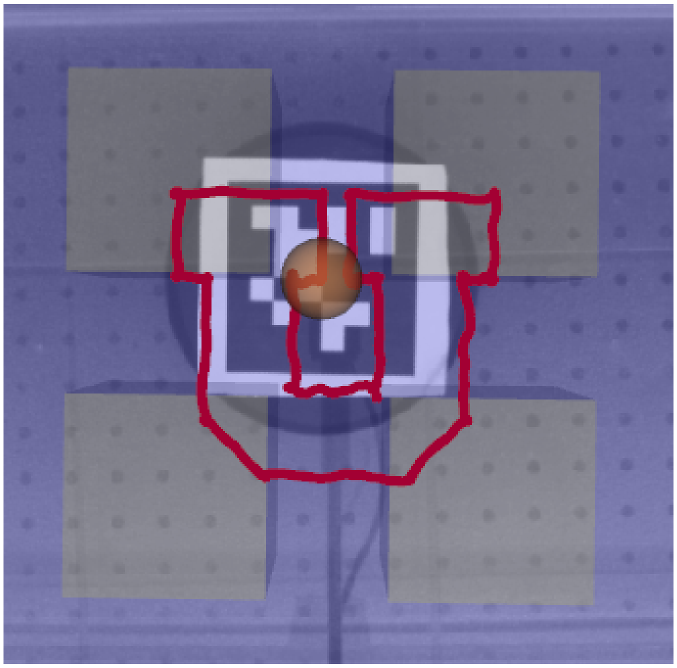

Fig. 1: Example trajectory—the University of Utah “Block U”—produced using the proposed continuous-position force-torque model. The red line represents position over time (72 minutes) traced by the center of a 20-mm-diameter copper sphere. In this planar simulation of microgravity, the copper sphere is placed in a raft that floats with 3-DOF mobility on the surface of water, with four electromagnetic field sources placed beneath the water tank. The pose of the raft is tracked with a camera using a fiducial marker. The positions of the field sources and the copper sphere are rendered in the image at true scale and with perspective; they are obstructed in the actual video.

The use of eddy-current-induced forces and/or torques for applications in space is a particularly promising and active area of research. This arises in part by the benefit of non-contact actuation in reducing the chances of destructive collision compared to contact-based approaches, and is further motivated by the large quantities of aluminum in engineered space objects [14]. For example, eddy-current-induced forces have been proposed as a method of traversing the exterior of the International Space Station [20, 26, 27, 28]. We are particularly interested in contributing solutions to the problem of space debris [7, 21, 10, 11]. A study found that "even if no future launches occurred, collisions between existing satellites would increase the 10-cm and larger debris population faster than atmospheric drag would remove objects" [11]. This will eventually lead to a phenomenon known as the Kessler Syndrome [6], in which Earth's orbit becomes clogged with debris due to cascading collisions between objects, making it unusable. As such, there is a dire need for remediation strategies to remove or repair resident space objects in order to protect the fast-growing number of satellites that the world's population has grown to rely on [11]. The majority of prior efforts have focused on eddy-current breaking for detumbling satellites [15, 25, 8, 13].

We recently showed that full six-degree-of-freedom (6-DOF) dexterous manipulation of conductive, nonmagnetic objects (specifically spheres) utilizing eddy currents is, in fact, possible [17]. The method assumes that the object is surrounded by static electromagnet field sources capable of generating continuously rotating magnetic dipole fields about arbitrary axes. It is noteworthy that the resulting manipulation was in full 6-DOF, whereas 6-DOF manipulation of ferromagnetic objects is only possible for complex geometries [3], with 5-DOF typical of most simple geometries, and only 3-DOF achievable for soft-magnetic spheres [1]. The forces and torques induced on conductive, nonmagnetic spheres are small compared to those due to ferromagnetism, but they have the potential to be useful for applications in the microgravity environment of space.

In this paper, we make five contributions relative to our earlier work [17], motivated by manipulation of space debris:

1) Pham et al. [17] modeled eddy-current-induced force-torque at three distinct canonical positions of a nonmagnetic, conductive sphere with respect to a rotating dipole: along the rotation axis of the rotating dipole (parallel and antiparallel) and orthogonal to the axis of rotation. Here, we provide a single, continuous model of force-torque across all positions of the conductive sphere relative to the rotating dipole.

2) Pham et al. [17] used the canonical-position model in a manipulation framework, which forced the conductive sphere to be cast into one of the three canonical positions during actuation. Although this method was sufficient to enable 6-DOF manipulation (provided there were enough dipole-field sources), it unnecessarily constrained the dipole rotation axes that could be used, making the results sub-optimal. Here, we modify the manipulation framework to use the new continuous-position model, and show improved tracking performance to that of [17], while solving a simpler optimization problem. Figure 1 shows an example trajectory experimentally generated with our improved method.

3) Pham et al. [17] assumed that object dynamics models were accurately known. As a step toward manipulation of unknown space debris, we propose an approach to manipulating spheres with unknown physical parameters (i.e., radius and conductivity) through the use of adaptive control. We leverage the recently proposed view of adaptive control as online optimization [19]. This enables us to more closely tie adaptive control to classical system identification [2], while also making use of exciting advances in online optimization [4] such as solvers that are robust to noise while also handling constraints and injecting prior knowledge of system parameters.

4) Pham et al. [17] only physically manipulated copper spheres. Here, we use the adaptive controller to enable the first physical demonstration of manipulation of aluminum spheres; aluminum is the most commonly used material in engineered space objects.

5) Pham et al. [17] developed a model for induced force-torque on nonmagnetic, conductive spheres, which was hypothesized to be a useful approximation for other geometries. Here, we demonstrate that our adaptive controller can be used to manipulate nonspherical, nonmagnetic, conductive objects by locally approximating the dynamics using the model for spheres. This constitutes the first demonstration of magnetic manipulation of nonspherical, nonmagnetic objects.

The paper structure continues as follows. We review the existing state-of-the-art force-torque model in Sec. II. We provide an explanation of our proposed continuous-position force-torque model in Sec. III. We discuss our manipulation framework in Sec. IV. We then detail our approach to object parameter optimization, both as system identification and adaptive control, in Sec. V. We share our experimental design and results in Sec. VI before concluding in Sec. VII.

II. Review of Existing Force-Torque Model

In this section, we summarize the model of Pham et al. [17]. However, we recast the model into spherical coordinates, which we have found enables an elegant way to extend the existing model to new, previously unmodeled locations.

The magnetic field source can be abstracted as a point dipole $\boldsymbol{m}$ (units A·m^2, with direction pointing from the south pole to the north pole) at its center of mass. The center of the nonmagnetic conductive sphere is then described by a relative displacement vector $\boldsymbol{\rho}$, with both vectors expressed in a common frame of reference. Figure 2 shows the new spherical coordinate system, where any given position can be described by three coordinates with respect to the rotating magnetic dipole: a distance $\rho = \|\boldsymbol{\rho}\|$, a polar angle θ measured from the dipole's rotation vector $\boldsymbol{\omega}$, and an azimuthal angle ϕ measuring a right-handed rotation about $\boldsymbol{\omega}$. In this coordinate system, the three canonical positions from [17] are described by $\theta = 0^\circ$, $\theta = 90^\circ$, and $\theta = 180^\circ$.

The eddy-current-induced force f and torque τ was empirically modeled, using both finite-element analysis (FEA) and experiments, at the three canonical positions as a function of the magnetic dipole strength $m = \|\boldsymbol{m}\|$, the dipole rotation frequency $\omega = \|\boldsymbol{\omega}\|$ (units Hz), the radius r (units m) of

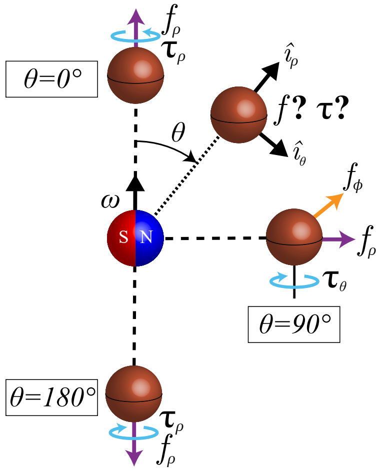

Fig. 2: Eddy-current-induced forces and torques shown in a spherical coordinate system to describe arbitrary positions relative to a rotating dipole source. Note that $\hat{\imath}_\phi = \hat{\imath}_\rho \times \hat{\imath}_\theta$. The three canonical positions in [17], and their respective forces and torques, are recast in the spherical coordinate system. The arrowhead on $\boldsymbol{\tau}_\rho$ at 180° depicts the positive sign convention, which is opposite to the actual torque direction for the $\boldsymbol{\omega}$ shown. All other force/torque arrowheads depict both the positive sign convention and the actual force/torque direction for the $\boldsymbol{\omega}$ shown. The model makes no estimate of force/torque at other positions, such as those denoted by f**?** and $\boldsymbol{\tau}$**?**.

the conductive sphere, the distance ρ, and the electrical conductivity σ (units S/m) of the conductive sphere:

$$f,\tau = \frac{\left(c_0\sigma\mu_0\omega r^2\right)^{c_1\left(\sigma\mu_0\omega r^2\right)^{c_2}} 10^{c_3}\left(\mu_0 m^2\right)}{\left(\frac{\rho}{r}\right)^{c_4} r^{c_5}} \tag{1}$$

where $\mu_0 = 4\pi \times 10^{-7}\,\mathrm{N{\cdot}A^{-2}}$ is the permeability of free space. The coefficients for the $\theta = 0°$ and $\theta = 90°$ positions—which is all that we will need going forward, due to the symmetry of $\theta = 0°$ and $\theta = 180°$—are provided in Table I. Pham et al. [17] recommended using both the experimentally derived coefficients and FEA-derived coefficients to bound the estimates on the resulting force and torque. The force-torque model is quasistatic, as it was empirically derived using a static conductive sphere.

The model in Eq. (1) is accurate in a "far-field" regime in which the center of the nonmagnetic sphere is approximately 1.5 sphere radii or farther away from the center of the magnetic field source ($\rho > 1.5r$). This is not a particularly restrictive assumption, considering that the theoretical lower limit on ρ is $\rho = r$ (for a point dipole) and any actual magnetic field source has its own finite dimensions. In the "near-field" regime ($\rho \le 1.5r$), the model Eq. (1) underpredicts the force-torque magnitude, and as such is in a sense conservative. In practice, the near-field regime applies to scenarios in which the physical magnetic field source is close to a much larger nonmagnetic, conductive object.

III. CONTINUOUS MODEL OF INDUCED FORCE & TORQUE

In this section, we expand the force-torque model from the previous section to arbitrary locations (but still in the far-field regime) of a conductive sphere in a rotating dipole field. Our guiding hypothesis is that there will exist simple (likely trigonometric) functions of θ that will enable us to (nonlinearly) interpolate the modeling results in the three canonical positions, such that no further modeling of the type given in Eq. (1) will need to be conducted.

TABLE I: Coefficients from [17] for model in Eq. (1) for canonical positions, recast in spherical coordinates; see Fig. 2

θ	$f,\ \tau$	Coefficients					
FEA Simulations							
		c_0	c_1	c_2	c_3	c_4	c_5
0°	f_ρ	430	2.95	−0.101	−9.26	7	4
0°	τ_ρ	6840	3.00	−0.0986	−13.2	6	3
90°	f_ρ	266	2.60	−0.101	−7.65	7	4
90°	f_ϕ	6040	3.45	−0.102	−14.3	7	4
90°	τ_θ	8100	3.60	−0.0985	−15.7	6	3
Experiments							
θ	$f,\ \tau$	Coefficients					
		c_0	c_1	c_2	c_3	c_4	c_5
0°	f_ρ	467	2.81	−0.0969	−9.75	7	4
0°	τ_ρ	6900	3.35	−0.0990	−14.9	6	3
90°	f_ρ	282	3.20	−0.0980	−9.41	7	4
90°	f_ϕ	5870	3.49	−0.0973	−14.6	7	4
90°	τ_θ	8000	3.40	−0.0928	−15.0	6	3

We conducted new simulations of magnetically induced forces using Ansys multiphysics FEA, following the specifications provided in [17] (see Appendix A). We placed the conductive sphere relative to the rotating dipole source from $\theta = 0°$ to $\theta = 180°$ at 15° increments, as shown in Figs. 3(a) and 3(c). Our simulation had a dipole strength $m = 200\,\mathrm{A{\cdot}m^2}$, a dipole rotation frequency $\omega = 10\,\mathrm{Hz}$, a conductive-sphere radius $r = 50\,\mathrm{mm}$, a distance $\rho = 500\,\mathrm{mm}$, and conductive-sphere electrical conductivity of $\sigma = 5.8 \times 10^7$ S/m for copper.

The complete results of the FEA are shown in Fig. 3, with the exception that components in the $\hat{\imath}_\phi$ direction are not depicted in Figs. 3(a) and 3(c). From these results, it became evident that all six force and torque components can be expressed by simple trigonometric functions that provide a smooth transition between the modeled forces and torques at the three canonical positions to arbitrary values of θ, and that also embody the symmetries that we would expect. The equations that describe the force and torque components in spherical coordinates—at arbitrary values of ρ and θ, and not requiring ϕ due to symmetry—which call the canonical-position model of Eq. (1), are as follows:

$$f_\rho(\rho,\theta) = -\left(\frac{f_\rho(\rho,90°) - f_\rho(\rho,0°)}{2}\right)\cos(2\theta) + \left(\frac{f_\rho(\rho,90°) + f_\rho(\rho,0°)}{2}\right) \tag{2}$$

$$f_\theta(\rho,\theta) \approx 0 \tag{3}$$

$$f_\phi(\rho,\theta) = f_\phi(\rho,90°)\sin(\theta) \tag{4}$$

$$\tau_\rho(\rho,\theta) = \tau_\rho(\rho,0°)\cos(\theta) \tag{5}$$

$$\tau_\theta(\rho,\theta) = \tau_\theta(\rho,90°)\sin(\theta) \tag{6}$$

$$\tau_\phi(\rho,\theta) = 0 \tag{7}$$

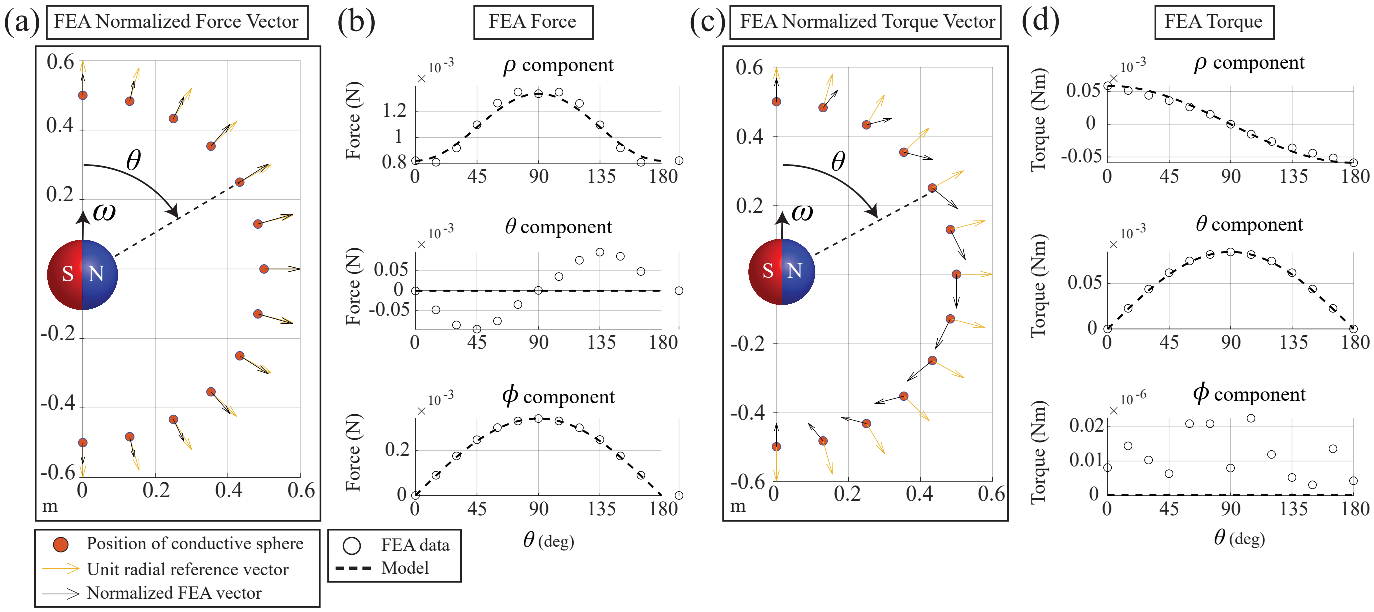

Fig. 3: Complete results of FEA. (a) Force vectors in the $\hat{\imath}_\rho$-$\hat{\imath}_\theta$ plane for each conductive-sphere position, normalized by the value of f_ρ at $\theta = 90^\circ$ (i.e., the maximum value). A $\hat{\imath}_\rho$ unit vector is shown in yellow for reference. (b) Three components of force vector as a function of θ, with trigonometric models (dashed lines) given by Eqs. (2–4), respectively. (c) Torque vectors in the $\hat{\imath}_\rho$-$\hat{\imath}_\theta$ plane for each conductive-sphere position, normalized by the value of τ_θ at $\theta = 90^\circ$ (i.e., the maximum value). A $\hat{\imath}_\rho$ unit vector is shown in yellow for reference. (d) Three components of torque vector as a function of θ, with trigonometric models (dashed lines) given by Eqs. (5–7), respectively.

Our decision to model $\tau_\phi = 0$ comes from the observation that the simulation results appear to simply be numerical noise with no discernible pattern. The data produce none of the symmetry we would expect from a magnetic model and exhibit magnitudes three orders of magnitude smaller than the other torque components.

Our decision to model $f_\theta \approx 0$, even though Fig. 3(b) suggests that f_θ is also described by a trigonometric function, is based on two considerations. First, it is evident from Fig. 3(a) that forces in the $\hat{\imath}_\rho$-$\hat{\imath}_\theta$ plane are almost entirely in the $\hat{\imath}_\rho$ direction, such that ignoring the force component in the $\hat{\imath}_\theta$ direction will likely have a negligible impact on our ability to perform manipulation. Second, whereas the other five force-torque components could be modeled as a bridge between the values at the canonical positions, in the case of f_θ the value at the canonical positions is zero. Consequently, finding the value of f_θ at $\theta = 45^\circ$ would require additional modeling, analogous to the efforts of Pham et al. [17] that led to the model in Eq. (1). Since the negligibility of f_θ may be system/configuration dependent, modeling of f_θ may be justified in future work. For now, we will proceed with the assumption that closed-loop control will correct for any modeling deficiencies.

IV. MANIPULATION FRAMEWORK

We now propose a control framework to perform dexterous manipulation with multiple dipole-field sources (partially) surrounding the conductive object, using the force-torque model of Section III. We assume we are given a time-varying force-torque profile to track. In practice, we generate this by planning a desired trajectory for the object with bounded velocity and acceleration and use a simple PD controller to derive the target wrenches. Our problem then becomes how to achieve a given desired wrench.

We assume that each source is an electromagnet capable of dipole rotation about any axis (e.g., an Omnimagnet [16]). Both m and $\boldsymbol{\omega}$ can be controlled, but their maximum achievable magnitudes are coupled due to the low-pass-filtering effect of induction in the electromagnets; that is, an increase in ω results in a decrease in the maximum value of m that can be achieved before the amplifiers' voltage limits are reached. As in [17], we have chosen to treat m and the direction of $\boldsymbol{\omega}$ (i.e., the unit vector $\hat{\boldsymbol{\omega}}$) as the control variables, and to use a constant rotation frequency ω, which simplifies our control problem but somewhat limits the peak tracking performance of the controller. We assume n electromagnets, with the i^{th} electromagnet located at position $\mathscr{P}_i$. We assume a single conductive object at pose $\boldsymbol{x}$ comprising a position $\mathscr{P}_c$ and orientation R_c [9]. We can describe the conductive object by a displacement vector $\boldsymbol{\rho}_i = \mathscr{P}_c - \mathscr{P}_i$ with respect to each dipole source, where $\rho_i = \|\boldsymbol{\rho}_i\|$.

For each electromagnet, we parameterize the control variable $\hat{\boldsymbol{\omega}}$ with respect to the world frame (i.e., a common frame of reference) using spherical coordinates, with a polar angle ψ measured from from the z-axis, and an azimuthal angle ξ measured about the z-axis and from the x-axis (see Fig. 4). Given a pair $(\psi,\ \xi)$, we can reconstruct

$$\hat{\boldsymbol{\omega}} = \begin{bmatrix} \sin(\psi)\cos(\xi) \\ \sin(\psi)\sin(\xi) \\ \cos(\psi) \end{bmatrix} \tag{8}$$

The angle θ can then be found using knowledge of $\hat{\boldsymbol{\omega}}$ and the $\boldsymbol{\rho}$ value for the electromagnet under consideration:

$$\theta = \operatorname{atan2}\left(||\hat{\boldsymbol{\omega}} \times \boldsymbol{\rho}||, \hat{\boldsymbol{\omega}} \cdot \boldsymbol{\rho}\right) \tag{9}$$

Let us first consider the special cases when $\theta = 0^\circ$ or $\theta = 180^\circ$, where only the radial force-torque components are nonzero. We construct a unit vector

$$\hat{\boldsymbol{\imath}}_\rho = \frac{\boldsymbol{\rho}}{\rho} \tag{10}$$

and then use Eq. (1) to solve for the induced force and torque on the conductive sphere:

$$\boldsymbol{f} = f_\rho(\rho, \theta)\hat{\boldsymbol{\imath}}_\rho \tag{11}$$

$$\boldsymbol{\tau} = \tau_\rho(\rho, \theta)\hat{\boldsymbol{\imath}}_\rho \tag{12}$$

For all other values of θ, we can construct unit basis vectors that are compatible with the model of Section III:

$$\hat{\boldsymbol{\imath}}_\phi = \frac{\hat{\boldsymbol{\omega}} \times \boldsymbol{\rho}}{\|\hat{\boldsymbol{\omega}} \times \boldsymbol{\rho}\|} \tag{13}$$

$$\hat{\boldsymbol{\imath}}_\theta = \hat{\boldsymbol{\imath}}_\phi \times \hat{\boldsymbol{\imath}}_\rho \tag{14}$$

where $\hat{\boldsymbol{\imath}}_\rho$ is calculated as in Eq. (10). The induced force and torque on the conductive sphere is then:

$$\boldsymbol{f} = f_\rho(\rho, \theta)\hat{\boldsymbol{\imath}}_\rho + f_\theta(\rho, \theta)\hat{\boldsymbol{\imath}}_\theta + f_\phi(\rho, \theta)\hat{\boldsymbol{\imath}}_\phi \tag{15}$$

$$\boldsymbol{\tau} = \tau_\rho(\rho, \theta)\hat{\boldsymbol{\imath}}_\rho + \tau_\theta(\rho, \theta)\hat{\boldsymbol{\imath}}_\theta \tag{16}$$

For ease of notation, we refer to this as our wrench model $\boldsymbol{f}, \boldsymbol{\tau} = w(\boldsymbol{x}, \boldsymbol{\lambda}, \boldsymbol{\eta})$, where $\boldsymbol{\lambda}$ denotes a set of object parameters (e.g., sphere radius and conductivity) and $\boldsymbol{\eta} = \{i, m, \psi, \xi\}$ denotes the control parameters.

No closed-form inverse exists for the wrench model. Instead, for some instantaneous object pose and given set of object parameters we can solve the following constrained optimization problem to select the dipole field source and associated dipole strength and axis of rotation that produces a wrench as close as possible to the desired wrench:

$$\begin{aligned} \underset{i,m,\psi,\xi}{\operatorname{argmin}} \quad & \left\| \begin{bmatrix} \boldsymbol{f}_{\text{des}} \\ \boldsymbol{\tau}_{\text{des}} \end{bmatrix} - \begin{bmatrix} \boldsymbol{f} \\ \boldsymbol{\tau} \end{bmatrix} \right\|_{\boldsymbol{Q}}^2 \\ \text{s.t.} \quad & i \in \{1, \cdots, n\} \\ & m \in [0, m_{\max}] \\ & \psi \in [0, \pi] \\ & \xi \in [-\pi, \pi] \\ & \boldsymbol{f}, \boldsymbol{\tau} = w(\boldsymbol{x}, \boldsymbol{\lambda}, \{i, m, \psi, \xi\}) \end{aligned} \tag{17}$$

where the $\boldsymbol{Q}$-norm enables relative weighting between force and torque (which have different units). Reformatting $\hat{\boldsymbol{\omega}}$ as the pair (ψ, ξ) lets us construct the optimization without needing nonlinear constraints enforcing $\hat{\boldsymbol{\omega}}$ to be a unit vector.

We can efficiently find the optimal inputs using a parallelized (two initializations for each of the n electromagnets) Newton-method solver. We handle bound constraints through projection using a backtracking line-search [12]. For our system we set $m_{\max} = 40\,\text{A}{\cdot}\text{m}^2$.

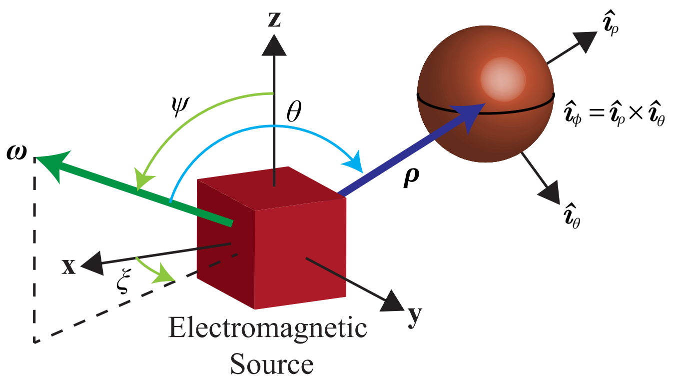

Fig. 4: Spherical coordinate systems describing the dipole rotation vector $\boldsymbol{\omega}$ with respect to the world frame, and the conductive sphere with respect to $\boldsymbol{\omega}$ (as in Fig. 2).

V. ADAPTIVE CONTROL SCHEME

The model and control framework that we proposed in the previous sections expand the space of possible wrenches that we can induce compared to previous work, but they still require that the object being manipulated is a sphere of known properties. We aim to explore to what extent we can relax this assumption through the use of an adaptive control framework. Our hope is that, not only will this approach enable us to identify the parameters of spherical objects, but will also enable manipulation of nonspherical objects by identifying online a spherical approximation that describes the observed behavior of the object.

We now formalize the system identification and adaptive control problem, which aims to find the optimal physical parameters of a sphere, $\boldsymbol{\lambda}^*$, given a discrete, time-varying sequence of object poses and input controls $\Omega = (\boldsymbol{x}[0], \boldsymbol{\eta}, \ldots, \boldsymbol{x}[K], \boldsymbol{\eta}[K])$ with time horizon K. Unlike the empirical model of wrenches induced in spheres, which was derived using wrench measurements, we now assume at the time of deployment that we only observe the object pose. Although many modalities (e.g., lidar, radar, GPS) could be used to determine object pose in practice, we use visual observations in our experiments. We use an online smoothing formulation to track the object deriving less noisy pose estimates as well as associated object velocities $\dot{\boldsymbol{x}}[k]$. In our wrench model, the free model parameters $\boldsymbol{\lambda}$ are the spherical radius, r, and electrical conductivity, σ. We can estimate the mass matrix, $M(\boldsymbol{\lambda})$ of a solid sphere with radius r given an estimate of its density ρ.

We can connect these observed data with our magnetic wrench model, w, and thus our control inputs, by imposing a rigid-body motion model on the object dynamics. Given our target domain of space debris, our motion model assumes no friction and a simple linear mapping between the applied wrench and the resulting acceleration (i.e., Newton's second law). To solve for the parameters of our model as an optimization problem, we must define an associated loss (i.e., error) function over the observed data and dynamic object parameters. We consider two loss formulations. The first is the inverse dynamics or acceleration-based loss formulation

$$\mathscr{L}_a(\boldsymbol{\lambda},k) = \left\| \left(\frac{\dot{\boldsymbol{x}}[k+1]-\dot{\boldsymbol{x}}[k]}{\delta t}\right) - M(\boldsymbol{\lambda})^{-1} w(\boldsymbol{x}[k],\boldsymbol{\lambda},\boldsymbol{\eta}[k]) \right\|_{\boldsymbol{Q}}^2, \tag{18}$$

where δt is the controller's update period. The second is the forward dynamics or force-based loss formulation

$$\mathscr{L}_f(\boldsymbol{\lambda},k) = \left\| M(\boldsymbol{\lambda}) \left(\frac{\dot{\boldsymbol{x}}[k+1]-\dot{\boldsymbol{x}}[k]}{\delta t}\right) - w(\boldsymbol{x}[k],\boldsymbol{\lambda},\boldsymbol{\eta}[k]) \right\|_{\boldsymbol{Q}}^2. \tag{19}$$

In both cases we use finite differencing to estimate the acceleration from the observed object velocities. The weights used in the two $\boldsymbol{Q}$-norms would be different in general. Using either loss formulation, we can construct the batch system identification problem [2] as the following optimization:

$$\boldsymbol{\lambda}^* = \underset{\boldsymbol{\lambda}}{\operatorname{argmin}} \sum_{k=0}^{K-1} \mathscr{L}(\boldsymbol{\lambda},k) \tag{20}$$

We investigate this batch formulation as a baseline in our experiments below. However, our primary interest lies in identifying the object parameters online. It is not obvious how to generate a safe set of controls to collect the data for system identification when the object properties are unknown. This motivates our adaptive control formulation.

In adaptive control we leverage our model-based control to define the control signal, while updating the estimate of $\boldsymbol{\lambda}$ online based on our observations. Typically, in performing adaptive control, we would not fully solve this optimization at each step, but instead perform a single gradient step to update the parameters:

$$\boldsymbol{\lambda}[k+1] = \boldsymbol{\lambda}[k] - \alpha_k \nabla_{\boldsymbol{\lambda}} \mathscr{L}(\boldsymbol{\lambda}[k],k) \tag{21}$$

with some step length α_k [23, 22]. However, by framing the adaptive controller as an online optimization problem [19] we can use a broad set of tools in deciding on how to solve for the system parameters. In particular we wish to explicitly model bound constraints on our object parameters and examine different solvers including the momentum optimizer that has been shown to improve performance over gradient descent by smoothing out oscillations [18]. We can additionally examine mini-batch formulations of the optimization where we use the most recent k timesteps of pose and control data instead of the full batch as traditionally done in system identification or only a single step as traditionally done in adaptive control. In our experiments we select our step length, α_k online using the same backtracking line search used in our controller, and handle constraints using the same projection approach [12]. We give further details of the design choices we examined for solving the adaptive control problem, including the performance of the different loss functions, in the following section.

VI. EXPERIMENTS

We now provide details of our experiments and their results. Pham et al. [17] used numerical simulation to demonstrate that 6-DOF manipulation is possible with the limited model, as constructing a microgravity simulation to physically validate the manipulation in 6-DOF was infeasible. To demonstrate the model is sufficiently accurate on objects in quasistatic motion and under closed-loop control, Pham et al. [17] constructed a 3-DOF (2-DOF translation + 1-DOF orientation) physical, microgravity simulation on the surface of water. As we focus on generalizing this prior work to more control actions and object types, we focus on physical experiments in the same microgravity simulator. We only use numerical simulation to explore design decisions. In the next section we describe the physical microgravity simulation environment we use for model and control validation. Following that, we show manipulation results using our novel continuous-position model of magnetically induced force and torque in conductive, nonmagnetic objects. Our experiments show results for both copper and aluminum spheres. We then provide comparative analysis of our two proposed system-identification loss functions using data collected in numerical simulation. Finally, we provide extensive results of our adaptive controller using the physical simulator, including with nonspherical objects. Code, data, and videos associated with the experiments can be found at https://sites.google.com/gcloud.utah.edu/adaptiveeddycurrent.

A. *Physical Microgravity Simulation Environment*

We preformed physical experiments using the same system used in [17] with four Omnimagnets (i.e., omnidirectional electromagnets) placed beneath a water tank. Figure 1 provides a top-down view of the environment. The Omnimagnets can each produce an approximate dipole source rotating about an arbitrary axis to match the fully continuous ω produced by our controller. This produces a low-drag environment where forces act linearly on acceleration, thus acting similar to dynamics under microgravity in the plane. We placed a camera above the water tank to detect a fiducial marker placed on top of a plastic raft with the object of interest inside and rigidly connected to the raft. We solve a smoothing problem online to decrease noise from the instantaneous marker locations and estimate the object velocity. We show the conductive, nonmagnetic objects used in our experiments in Fig. 5.

B. *Validation of Continuous-Position Force-Torque Model*

Here, we validate our force-torque model introduced in Section III by reproducing the trajectory tracking experiments from [17] using the novel model. This task requires the system to control the object of interest to track a 3-DOF planar Cartesian trajectory to draw a square, while reorienting the object to point in the direction of motion each time it reaches a corner and maintain a fixed heading during motion along the edge of the square. We performed 5 trial experiments manipulating a copper sphere. For these experiments, we provide an accurate set of physical parameters to the model. In addition, we preformed 5 trials performing the Block-U trajectory while maintaining a constant orientation; the results of one of these trials is shown in Fig. 1. We find qualitatively that the controller tracks the desired trajectory well, correcting for slight deviations in position and orientation from the target

Fig. 5: The four objects used in our manipulation experiments: (back, left) a solid aluminum sphere of radius 20.0 mm, (back, right) a solid copper sphere that we approximate as having a radius of 20 mm but by mass-density has an effective radius of 19.8 mm, (front, left) a piece of aluminum scrap approximately cylindrical in shape with radius 25.2 mm and length of 23.1 mm with a hole in the center that is counterbored from one side, and (front, right) a solid, elongated copper cuboid with length 50 mm cut from a 25.4 mm square stock.

trajectory. Quantitatively, we examine the absolute tracking error in terms of both position and orientation across all of the square tracking experiments as the average error across all timesteps for each trial. Fig. 6 shows the distribution of average error across the trials. We see that the controller using our proposed continuous model achieves a substantial improvement over the results of the model in [17] (compare “Copper Pham et al.” and “Copper known object”), while solving a simpler optimization problem.

C. Acceleration-Based Loss Is Better than Force-Based Loss

We conducted a series of numerical simulations in 6-DOF using our proposed model to examine optimization choices for system identification and adaptive control. Our primary objective was to examine which of our proposed loss functions performed best when estimating the radius and conductivity of the sphere being manipulated. To this end, we computed both losses with varying values of sphere radius in the batch system-identification setting. We visualize the log-loss for both functions in Fig. 7. We see that the acceleration-based loss has a single minimum within the feasible range of radii, which coincides with the true radius of 0.02 m. The force-based loss on the other hand has a local minimum at the true radius and a global minimum at 0 radius as both the force and mass-matrix M decay to zero. With the force-based loss there is a substantial region where the gradient points towards the global minimum at 0 instead of the true radius and local minimum. As such, we elect to use the acceleration-based loss for all subsequent experiments to avoid the degenerate solution at 0.

We conducted further numerical simulations with varying levels of additive Gaussian noise on the observed object pose to design our optimization for online adaptive control. We found that using a mini-batch of the most recent 25 pose observations worked well in estimating the gradient in Eq. (21). We conduct a single gradient update step at each iteration of the control loop, selecting the update step length using a backtracking line search.

We found these settings made a good trade-off between being responsive to changes in the underlying dynamics parameters (created by abruptly shifting the simulated object radius to a new value), while still suppressing control errors induced from the noisy observations. Although several solvers were able to converge to the true radius while tracking the target trajectory (e.g., Newton’s method, Gauss-Newton), we

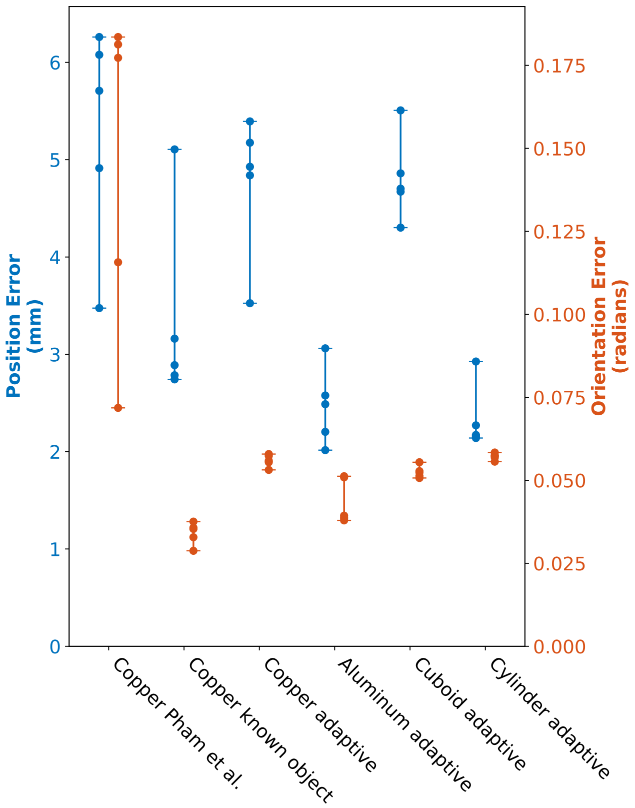

Fig. 6: Tracking error for each manipulation experiment. Points average absolute error per trial, bars show minimum and maximum values, across 5 trials. Results are for: copper sphere using method from Pham et al. [17], copper sphere using proposed method and known object parameters, copper sphere using adaptive control, aluminum sphere using adaptive control, copper cuboid using adaptive control, and aluminum cylinder using adaptive control.

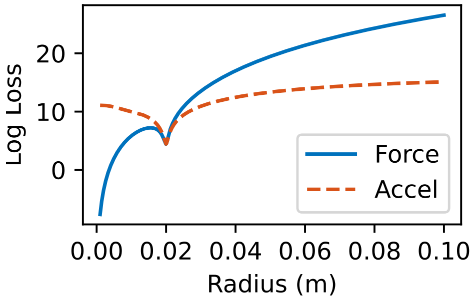

Fig. 7: Natural log of the total loss computed using force-space versus acceleration-space formulations of the object parameter loss. True radius is 0.02 m.

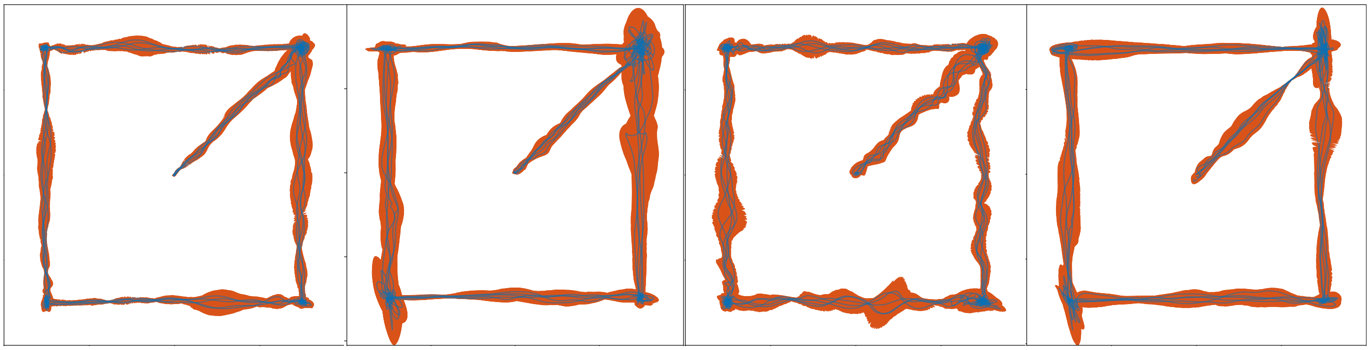

(a) Aluminum Sphere **(b)** Copper Sphere **(c)** Aluminum Cylinder **(d)** Copper Cuboid

Fig. 8: Adaptive control results on different objects. Black shows individual trials and blue the mean trajectory while red shading shows 95 percent confidence path computed given 5 trials per object. Units are in meters.

elected to use the momentum strategy [18] for all subsequent physical-system experiments, given its strong performance on our tests and those reported by Ratliff et al. [19].

As a final validation of these choices, we solved the batch system-identification problem (i.e., offline) of finding the sphere's radius on the data collected in the physical system experiments above. We found in the presence of observation noise and calibration error across 5 trials of the Block-U trajectory the estimated radius converged to $\{19.9, 21.3, 21.2, 20.6, 20.4\}$ mm, and across 5 trials of the square trajectory radius estimates converged to $\{16.8, 18.3, 18.8, 19.0, 19.7\}$ mm. The measured radius of the sphere is 19.8 mm. In these trials, conductivity converged within 1% of its initial value, which had been initialized to the conductivity of copper.

D. Adaptive Control of Unknown Spheres

We validate our adaptive controller by running 5 trials each on the copper and aluminum spheres shown in Fig. 5. In each trial, we examine optimizing over both the radius and electrical-conductivity parameters of the model. We initialized the parameters by setting the radius, $r = 0.01$ m, the electrical conductivity to the true value for copper, $\sigma_c = 5.800E+07$ S/m, and the density to that of copper, $\rho_c = 8940\,\mathrm{kg/m^3}$. Even the aluminum sphere was set with fixed density of copper and initialized with conductivity of copper. Additionally of note is the bound constraint on the object's radius which was set to $r \geq 0.01$ m. We include the mass matrix of the raft, M_b, with the estimated mass of the object, $M_o(\boldsymbol{\lambda})$, in the inverse dynamics model to remove its effects on control, $M(\boldsymbol{\lambda}) = M_b + M_o(\boldsymbol{\lambda})$. However this value does not enter into our force-torque model. We estimate the mass matrix of the object from its inferred radius as $M_o = \mathtt{diag}(m_o, m_o, m_o, h_o, h_o, h_o)$, with $m_o = \rho_c \frac{4}{3}\pi r^3$ and $h_o = \frac{2}{5} m_o r^2$.

We visualize tracking performance for all trials of the spherical objects in Figs. 8(a) and 8(b). Quantitatively, we find that tracking performance is comparable to the performance for the known model (compare "Copper adaptive" and "Aluminum adaptive" to "Copper known object" in Fig. 6).

Fig. 9(a) visualizes a representative trial of adaptive control of the aluminum sphere. We show the time-varying value of

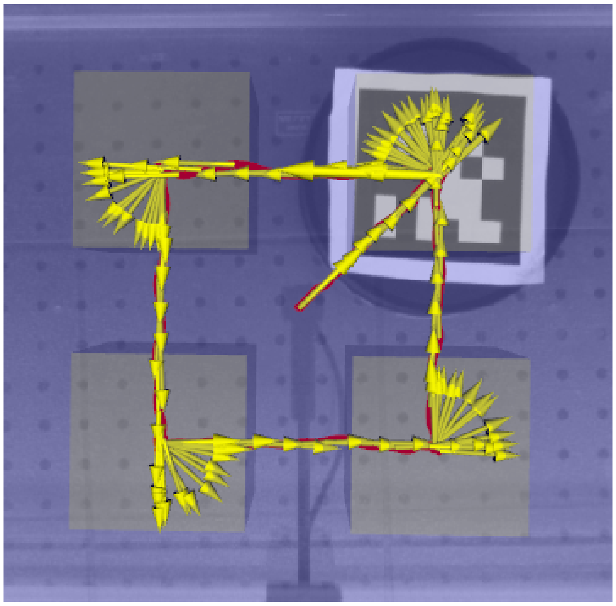

(a) Aluminum sphere single trial trajectory

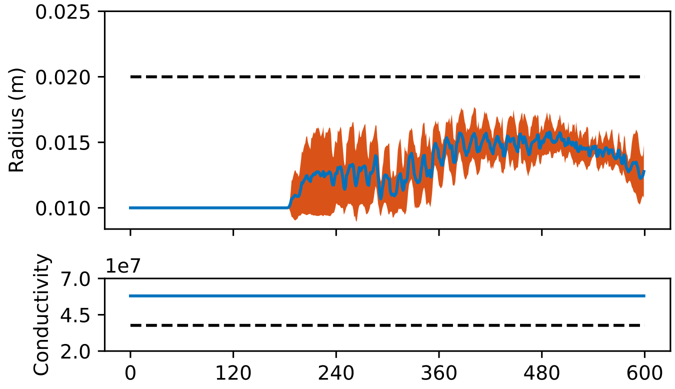

(b) Aluminum sphere adaptive parameters over time

Fig. 9: (a) Example trajectory produced by our adaptive controller manipulating an aluminum sphere. The red line represents position over time. Yellow arrows depict the object orientation, commanded to hold a fixed orientation along straight paths and to rotate in place at each corner. (b) Adaptive parameters over time for the first 10 minutes of each trial of the 40 minute trajectory. The blue line shows average parameter at timestep t and the orange region shows 1 standard deviation. The dashed black line represents the true value.

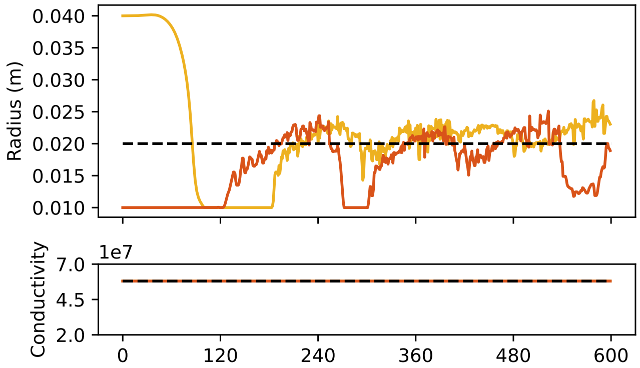

Fig. 10: Two trials of adaptive parameters over time for adaptive manipulation of a copper sphere. The yellow line shows a trial where the radius estimate was initialized to twice its true value, and the orange line shows a trial where the radius was initialized to half its true value. The dashed black line shows the true value.

the parameter estimates compared to their true values, across all trials, in Fig. 9(b). These results demonstrate that when conductivity is initialized much larger than its true value, the adaptive controller estimates a lower radius to compensate, rather than adapting conductivity. These results suggest that the control scheme is robust to inaccuracies in the underlying force-torque model. Further, since we primarily desired good control performance, we find the lack of precise parameter identification acceptable.

We further investigate our adaptive controller's robustness to different initializations by performing individual trials at a variety of initial conditions while manipulating a copper sphere. These results, shown in Fig. 10, demonstrate only slightly diminished performance by initializing with parameters that vastly over- or under-predict the generated wrenches.

E. Adaptive Control of Nonspherical Objects

Our final set of experiments test the hypothesis that the spherical model acts as a good first-order approximation for control of nonspherical objects. We investigate this by using our adaptive controller with the spherical-object model to manipulate nonspherical objects. We conducted 5 trials each on the elongated copper cuboid and the aluminum cylindrical objects shown in Fig. 5. We initialize the parameter estimates as in the previous experiment, with the density set to that of copper and the conductivity initialized to that of copper.

We visualize tracking performance for all trials with these object in Figs. 8(c) and 8(d). A characteristic trial of manipulation of the cuboid object is shown in Fig. 11, with the estimated sphere radius visualized at different times across the trajectory. We see that the controller never settles on a single estimate of the radius, instead adapting the value continuously based on the locally observed motion.

We see from Fig. 6 that, even though our force-torque model was built entirely from data derived from spheres, we achieve comparable tracking performance to that of the spheres when controlling objects with significantly nonspherical geometry.

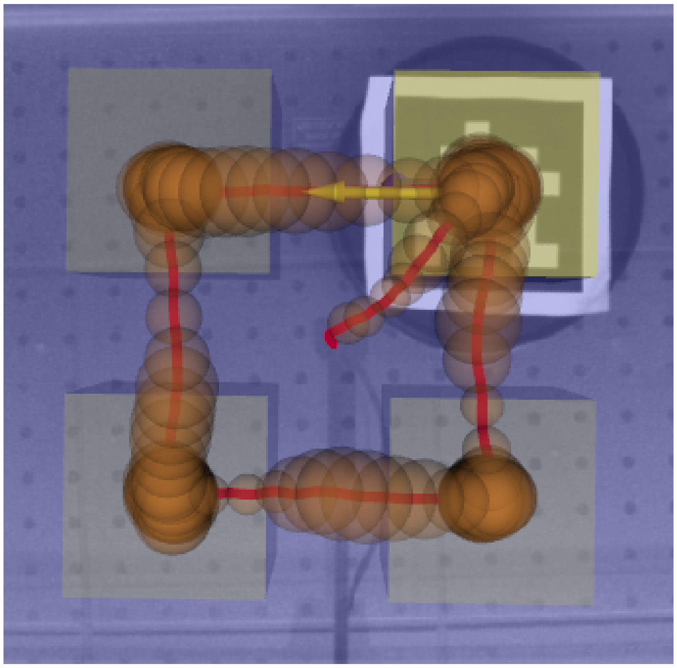

Fig. 11: Example trajectory produced by adaptive control of a copper cuboid. Periodically placed spheres visualize the radius estimate at different points along the trajectory. Note that no ground-truth radius exists for this nonspherical and anisotropic object. Instead the controller continuously adapts the radius in order to provide a locally correct model of dynamics.

VII. CONCLUSIONS AND FUTURE WORK

We have presented a novel, continuous model of magnetically induced forces and torques in nonmagnetic, conductive spheres. Our proposed model unifies the three discrete models previously proposed in [17], while also generalizing the model to arbitrary object positions, providing a larger space of forces and torques for use in downstream control tasks. We further validate an adaptive control technique for use of our novel model to control objects with unknown physical parameters and even nonspherical objects.

As future work we propose expanding the set of experimental objects, while also extending experiments to full 6-DOF microgravity simulations using submerged objects. We can further examine relaxing the assumptions of known object density in online mass matrix estimation. We also wish to examine combining forces from multiple magnetic sources simultaneously, which do not simply superimpose [17].

Our experiments validate our proposed model showing we can achieve better tracking performance than the previous model, while solving a computationally less expensive optimization problem. Using our proposed model and adaptive controller we demonstrate the first physical magnetic manipulation of aluminum spheres with unknown physical parameters and the first ever magnetic control of nonspherical, nonmagnetic objects. We see this as an important step toward manipulation of space debris, where we lack knowledge of exact physical models.

ACKNOWLEDGMENTS

This work was supported by the National Science Foundation under Grants 1841845 and 1846341. The authors would like to thank Rebecca Miles for her technical assistance.

REFERENCES

[1] Jake J. Abbott, Eric Diller, and Andrew J. Petruska. Magnetic Methods in Robotics. *Annu. Rev. Control Robot. Auton. Syst.*, 3:57–90, 2020.

[2] Christopher G. Atkeson, Chae H. An, and John M. Hollerbach. Estimation of Inertial Parameters of Manipulator Loads and Links. *Int. J. Robot. Res.*, 5(3):101–119, 1986.

[3] Eric Diller, Joshua Giltinan, Guo Z. Lum, Zhou Ye, and Metin Sitti. Six-degree-of-freedom Magnetic Actuation for Wireless Microrobotics. *Int. J. Robot. Res.*, 35(1–3): 114–128, 2016.

[4] Elad Hazan. Introduction to Online Convex Optimization. *Found. Trends Optim.*, 2(3–4):157–325, 2016.

[5] Heinrich Hertz. *Miscellaneous papers*, chapter II. On induction in rotating spheres. London: Macmillan, 1896. English translation by D. E. Jones and G. A. Schott.

[6] Donald J. Kessler, Nicholas L. Johnson, J.-C. Liou, and Mark Matney. The Kessler Syndrome: Implications to future space operations. *Adv. Astronaut. Sci.*, 137(8), 2010.

[7] J.-C. Liou and N. L. Johnson. Risks in Space from Orbiting Debris. *Science*, 311:340–341, 2016.

[8] Xiaoguang Liu, Yong Lu, Qiang Zhang, and Kemo Zhang. An application of eddy current effect on the active detumble of uncontrolled satellite with tilt air gap. *IEEE Trans. Magn.*, 55(12):1–11, 2019.

[9] Kevin M. Lynch and Frank C. Park. *Modern Robotics: Mechanics, Planning, and Control*. Cambridge University Press, Cambridge, UK, 2017.

[10] C. Priyant Mark and Surekha Kamath. Review of Active Space Debris Removal Methods. *Space Policy*, 47:194–206, 2019.

[11] National Aeronautics and Space Administration. Astromaterials Research & Exploration Science: Orbital Debris Program Office. https://orbitaldebris.jsc.nasa.gov/, 2021. Accessed: 2021-07-08.

[12] Jorge Nocedal and Stephen J. Wright. *Numerical Optimization*. Springer, New York, NY, USA, 2e edition, 2006.

[13] Mark A. Nurge, Robert C. Youngquist, and Stanley O. Starr. Drag and lift forces between a rotating conductive sphere and a cylindrical magnet. *Am. J. Phys.*, 86(6): 443–452, 2018.

[14] John N. Opiela. A study of the material density distribution of space debris. *Adv. Space Res.*, 43(7):1058–1064, 2009.

[15] Natalia Ortiz Gómez and Scott J. I. Walker. Eddy currents applied to de-tumbling of space debris: Analysis and validation of approximate proposed methods. *Acta Astronaut.*, 114:34–53, 2015.

[16] Andrew J. Petruska and Jake J. Abbott. Omnimagnet: An Omnidirectional Electromagnet for Controlled Dipole-Field Generation. *IEEE Trans. Magn.*, 50(7):8400810, 2014.

[17] Lan N. Pham, Griffin F. Tabor, Ashkan Pourkand, Jacob L. B. Aman, Tucker Hermans, and Jake J. Abbott. Dexterous Magnetic Manipulation of Conductive Non-magnetic Objects. *Nature*, 598:439–443, 2021.

[18] Ning Qian. On the momentum term in gradient descent learning algorithms. *Neural Netw.*, 12(1):145–151, 1999.

[19] Nathan Ratliff, Franziska Meier, Daniel Kappler, and Stefan Schaal. DOOMED: Direct Online Optimization of Modeling Errors in Dynamics. *Big Data*, 4(4):253–268, 2016.

[20] Benjamin Z. Reinhardt and Mason A. Peck. New Electromagnetic Actuator for On-Orbit Inspection. *J. Spacecraft Rockets*, 53(2):241–248, 2016.

[21] Minghe Shan, Jian Guo, and Eberhard Gill. Review and comparison of active space debris capturing and removal methods. *Prog. Aerosp. Sci.*, 80:18–32, 2016.

[22] Bruno Siciliano, Lorenzo Sciavicco, Luigi Villani, and Giuseppe Oriolo. *Robotics: Modelling, Planning and Control*. Springer-Verlag, 2009.

[23] Jean-Jacques E. Slotine and Weiping Li. *Applied nonlinear control*. Prentice hall Englewood Cliffs, NJ, 1991.

[24] York R. Smith, James R. Nagel, and Raj K. Rajamani. Eddy current separation for recovery of non-ferrous metallic particles: A comprehensive review. *Miner. Eng.*, 133:149–159, 2019.

[25] Fumihito Sugai, Satoko Abiko, Teppei Tsujita, Xin Jiang, and Masaru Uchiyama. Detumbling an uncontrolled satellite with contactless force by using an eddy current brake. In *IEEE/RSJ International Conference on Intelligent Robots and Systems*, pages 783–788, 2013.

[26] Katherine T. Wilson and Mason A. Peck. Electromagnetic, Free-Flying Mobility Relative to a Conductive Body. In *AIAA Scitech Forum*, 2020.

[27] Katherine T. Wilson and Mason A. Peck. Electromagnetic Actuation for Non-contact, Propellant-free, Six-Degree-of-Freedom Relative Mobility. In *AIAA Scitech Forum*, 2021.

[28] Katherine T. Wilson, Guadalupe Bernal, and Mason A. Peck. A Translating Eddy-Current Actuator for Relative Positioning of Spacecraft. In *AIAA Scitech Forum*, 2022.

APPENDIX A

In this appendix we describe how to setup Ansys Electronics Desktop 2019 R2 Maxwell to simulate the eddy-current-induced forces and torques on conductive copper spheres due to a rotating magnetic dipole as in Sec. III. The steps described in this appendix follow Pham et al. [17] directly. The order described below is in the same order as they would appear in the "Project Manager". Once the setup is performed for each configuration, force-torque data can be obtained by performing "Analysis All". In order to perform transient analysis with a rotating dipole source, one has to go to "Maxwell 3D", select "Solution Type" and choose "Transient".

Using `Coordinate System = Global`, we modeled the magnetic dipole source as a spherical NdFeB grade-N48 rare-earth magnet. When building the spherical magnet, it has the following model properties: `Command = Create Sphere, Coordinate System = Global, Center Position = [0, 0, 0]` (all model coordinates are provided in units of millimeters). The center of the sphere should be located at the center of the Global coordinate system. The material property for the spherical magnetic dipole has the following material properties: Relative Permeability $\mu_m/\mu_0 = 1.04$, Bulk Conductivity $\sigma = 714286\,\text{S/m}$, Magnetic Coercivity $H_{cm} = 1055931\,\text{A/m}$ (in Ansys this is entered as a negative value), `Core Loss = None, Composition = Solid, Mass Density =` $7550\,\text{kg/m}^3$, `Young's Modulus = Undefined, Poisson's ratio = Undefined,` and `Thermal Modifier = None`. The radius of the magnet was determined to achieve the desired dipole strength m, which is equal to the product of the remanent magnetization M_r and the volume of the sphere. Using a linear magnetization model, we can compute $M_r = H_{cm}\mu_m/\mu_0$. Also note that the default magnetization in Ansys is in the x direction.

To enable the dipole-source rotation, a regular polyhedron was created surrounding the magnet with the following model properties: `Coordinate = Global, Center Position = [0, -45, 0], Start Position = [0, 0, 0], Axis = Y, Height = 90`, and `Number of Segments = 100`.

To model the conductive sphere, a new coordinate system was created, which enables all relative sphere components to move together and output force-torque values to be referenced relative to the conductive-sphere frame. The model for the conductive sphere has the following properties: `Command = Create Sphere, Coordinate System = Sphere, Center Position = [0, 0, 0]`, and the desired radius. A conductive copper sphere has the following material properties: `Relative Permeability = 1, Bulk Conductivity = 58000000 S/m, Magnetic Coercivity = 0, Core Loss = 0, Composition = Solid, Mass Density = 8933 kg/m`^{3}`, Young's Modulus = 120000000000, Poisson's Ratio = 0.38, Thermal Modifier = None.`

A cubic box was created to surround the conductive sphere for refined meshing. It has the following model properties: `Command = Create Box, Coordinate System = Sphere`, with position and dimension of the box set such that the box was centered on the conductive sphere and had a side length that is 1% larger than the diameter of the sphere. It has `material property = air.`

Dipole rotation is implemented by right selecting the polyhedron model and assigning a Band. This generates a "MotionSetup" option under Model, which one can use to configure the following motion parameters: `Motion Type = Rotation, Coordinate System = Global, Axis = Y, Direction = Positive, Initial Position = 0 deg, Has Rotation Limit = unchecked`, and `Non Cylindrical = unchecked`. Under the "Mechanical" tab one can update the angular velocity to the desired frequency of rotation. This automatically generates a CylindericalGap mesh and the axis of the rotation vector must be along the same axis as the length of the polyhedron.

Output parameters are produced by right selecting the conductive sphere and creating parameters for force, torque in x, torque in y, and torque in z, with respect to the conductive sphere coordinate system. A single force parameter will automatically produce outputs for all x, y, z directions. Depending on the relative placement of the conductive sphere to the dipole rotation axis, one can transform the Cartesian coordinates to our proposed spherical coordinate system.

When assigning Mesh parameters, one must first right select the object and then select "Assign Mesh Operation". All mesh configurations have the following mesh properties: `Type = Length Based, Region = Inside Selection, Enable = checked, Restrict Length = checked`, and `Restricted Max Elems = checked`. Max Length and Max Elems are different for each object.

The mesh for the spherical permanent magnet is the mesh for the polyhedron. The polyhedron has `Max Length =` 5 mm and `Max Elements = 5000`. For the conductive sphere and its cubic box, the Max Length and Max Elems are scaled proportionally to r for consistent mesh properties across all conductive spheres. The simulated radius was $r = 50\,\text{mm}$. The mesh for the cubic box of air is an additional mesh operation for the conductive sphere and has `Max length =` $r/5\,\text{mm}$ and `Max Elems =` $50000r$.

In general, the Analysis setup consists of Stop Time and Time Step for each simulation and are listed here with respect to $\omega = 1\,\text{Hz}$ and `Time Step =` 1 ms. For this paper, a `Stop Time =` 2.5 was used. For any value of ω, the Analysis Setup parameters would be scaled proportional to each frequency in order to maintain the same number of data points and number of dipole rotations. For examples, a conductive sphere with 50 mm radius, at $\omega = 2\,\text{Hz}$, values would be updated to `Stop Time =` 1.5 s and `Time Step =` 0.5 ms.

Under "Results", create two transients reports of rectangular plots for force and torque output on the conductive sphere. Data is saved for each time step of the simulation.

To include the effects of eddy current on the conductive sphere, go to Maxwell 3D, select Excitations, select Set Eddy Effects, and check the box for the conductive sphere.

Once the setup is complete, one can perform "Analysis All" in order to start the simulations. While iterating through all parameters, simulations were automated through the use of a Python script using ANSYS Maxwell "Automation". Steady-state data was obtained by averaging the last dipole rotation.